




Article

Feasibility of 4D Gravity Monitoring in Deep-Water Turbidites Reservoirs

Andre D. Arelaro ^{1,2,*} , Valeria C. F. Barbosa ² , Vanderlei C. Oliveira Jr ²  and Paulo T. L. Menezes ^{1,3} ¹ Petroleo Brasileiro S.A. (Petrobras), Rio de Janeiro 20231-030, Brazil² Department of Geophysics, Observatório Nacional, Rio de Janeiro 20921-400, Brazil³ Departamento de Geologia Aplicada, Faculdade de Geologia, Universidade do Estado do Rio de Janeiro (UERJ), Rio de Janeiro 20550-900, Brazil

* Correspondence: andre.arelaro@gmail.com

Abstract: We present a seafloor 4D gravity feasibility analysis for monitoring deep-water hydrocarbon reservoirs. To perform the study, we have simulated the gravity effect due to different density and pore pressure distributions derived from a realistic model of a turbiditic oil field in Campos Basin, offshore Brazil. These reservoirs are analogs of several other passive-margin turbiditic systems located around the world. We considered four reservoir scenarios including and not including seafloor subsidence. Our results indicate that the gravity responses are higher than the feasible value of 3 μGal 12 years following the base survey. The area of maximum gravity anomaly corresponds to where we suppose hydrocarbon extraction occurs. A maximum seafloor subsidence of 0.6 cm was estimated, resulting in no detectable gravity effects. Our results endorse the 4D seafloor gravity acquisition as a beneficial tool for monitoring deep-water passive-margin turbiditic reservoirs.

Keywords: reservoir monitoring; 4D gravity; feasibility test



Citation: Arelaro, A.D.; Barbosa, V.C.F.; Oliveira Jr, V.C.; Menezes, P.T.L. Feasibility of 4D Gravity Monitoring in Deep-Water Turbidites Reservoirs. *Minerals* **2023**, *13*, 907. <https://doi.org/10.3390/min13070907>

Academic Editor: Georgy Cherkashov

Received: 25 April 2023

Revised: 24 May 2023

Accepted: 29 May 2023

Published: 5 July 2023



Copyright: © 2023 by the authors. Licensee MDPI, Basel, Switzerland. This article is an open access article distributed under the terms and conditions of the Creative Commons Attribution (CC BY) license (<https://creativecommons.org/licenses/by/4.0/>).

1. Introduction

Currently, the oil industry is seeking ultra-deep marine exploratory opportunities that can reach water depths of over 2000 m with sedimentary overloads of a few kilometers. In these scenarios, using geophysical methods as an imaging tool is challenging because the distance between sources and the sensor can be substantial and impacts data quality. In these cases, an effective way to reduce the signal amplitude loss is to place the geophysical sensors on the seafloor closer to the desired targets. Concerning gravity measurements, high-resolution instruments set on the seafloor can allow for hydrocarbon production monitoring through 4D (time-lapse) acquisitions [1–3].

Gravity acquisitions can be conducted in almost every type of environment. Regarding aquatic environments, gravimetric surveys have been performed since the 1940s. First in lakes and later in marine regions with shallow depths [4]; then, going to deeper and more complicated sites over the years. Land 4D gravity acquisitions have been performed for some decades with various purposes, from geothermal field studies to volcano monitoring, aquifer water storage, mine subsidence, tectonic and post-glacial isostatic movements, and hydrocarbon exploration and production [3,5,6]. Since the end of the 1990s, seafloor 4D gravity acquisitions have been performed in the shallow waters of the North Sea to monitor the fluid dynamics in hydrocarbon fields [3,7,8] and seafloor subsidence due to hydrocarbon production.

Once the gravimetric method is sensitive to mass variations, seafloor 4D gravity measurements can improve our understanding of fluid movements inside a reservoir. Moreover, it directly impacts hydrocarbon recovery and reduction of geological uncertainties such as mass variation estimation, reservoir water influx characterization, gas/oil or oil/water contact estimation, and CO₂ injection and storage. It can also contribute to a better and optimized drilling plan by diminishing the number of wells, substantially reducing the

costs of a hydrocarbon field development project [3,9–15]. Furthermore, if pressure gauges are settled with gravimeters on the seafloor, one can obtain information about seafloor movement due to oil production [3,8,11,16–18]. The measure of seafloor deformation is crucial to reduce the risks of human exposure and production facilities. At last, seafloor 4D gravity is a relatively fast, cost-effective, and environmentally friendly geophysical method that can be used complementary to 4D seismic surveys [3,5,8,9,15,18,19].

Several studies performed all over the world in the last two decades show the efficiency of the seafloor 4D gravity technique. These include feasibility studies, survey improvements, time-lapse gravity processing, application of inversion methods, use of borehole and gravity gradiometry information, and real data interpretation [7,10–12,16,17,19–27].

In deep and ultra-deep waters, as in the case of the largest Brazilian hydrocarbon fields, the seafloor 4D gravity survey is a technological challenge. In this scenario, it is necessary to evaluate the technical feasibility of using the seafloor 4D gravity surveys for hydrocarbon-field monitoring. Thus, this study focuses on the feasibility of the seafloor 4D gravity acquisition for monitoring hydrocarbon reservoirs and seafloor movement. By improving the work developed by [28], we have performed 4D forward gravity modeling of a typical passive-margin turbiditic reservoir at Campos Basin, offshore Brazil. We tested three scenarios with seafloor movement and another without this phenomenon. Using the feasible (threshold) limit of 3 μGal , which can be considered as a conservative value concerning recent seafloor 4D gravity acquisitions [15,18], results exhibit gravity responses higher than the feasible limit, which validate the seafloor 4D gravity survey for similar situations.

2. Materials and Methods

2.1. Gravity Anomalies and Seafloor Changes

Consider a marine sedimentary basin where the seafloor is the interface separating the water column from the basin sediments (Figure 1). We assume that the water column and the sediments are homogeneous, with constant densities ρ_w and ρ_s , respectively. Inside the sediment layer stands a hydrocarbon-producing reservoir, with known dimensions and time-variable bulk density $\rho_b(t)$ due to its function.

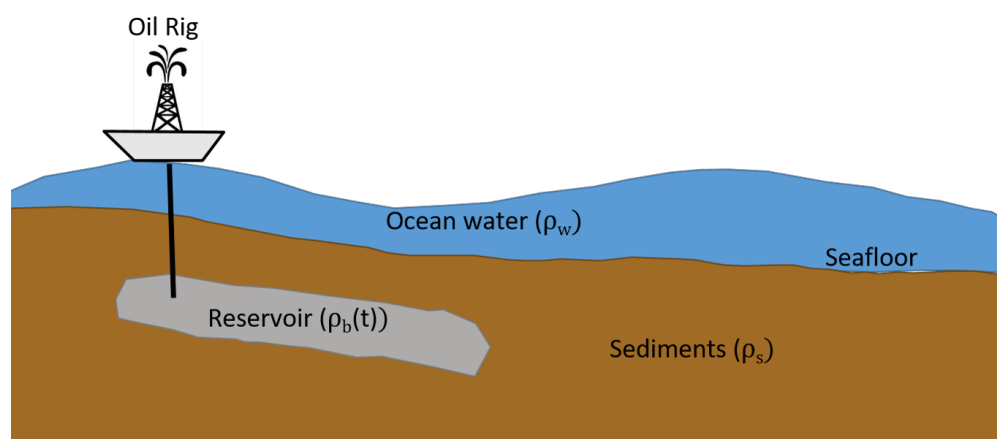


Figure 1. Sketch of a marine environment containing an ocean water layer (blue) with a constant density of ρ_w . Below the seafloor, there is a sedimentary layer (brown) with density ρ_s and a hydrocarbon-producing reservoir (gray) enclosed within the sediments, showing time-variable bulk density $\rho_b(t)$.

Let us simulate a seafloor 4D gravity survey over the model described in Figure 1. In this case, three phenomena can generate time-variable gravity anomalies: (1) water layer variation due to tides and waves; (2) reservoir mass variation due to hydrocarbon production; and (3) seafloor relief movement due to hydrocarbon production. The role of gravity modeling is to facilitate the study of the gravity response by isolating the gravity

effects caused by these phenomena. This work focuses on the 4D gravity effect yielded by the reservoir's mass variation and the seafloor movement due to hydrocarbon production. Thus, the 4D gravity effect of the ocean water movement has not been taken into account.

The gravity effect of a 3D density distribution can be calculated by dividing the study region in a sequence of vertical prisms adjacent in the three spatial directions with the x -axis to the north, y -axis rising to the east, and z -axis falling downward. From now on, this mesh of 3D vertical, juxtaposed prisms in the horizontal and vertical directions is called the interpretation model. The gravitational acceleration in the vertical direction $g_z(P_i, t_k)$ evaluated in a point $P_i = (x_i, y_i, z_i(t_k))$ representing the seafloor in a time t_k can be calculated according to Blakely [29]:

$$g_z(P_i, t_k) = \gamma \sum_{j=1}^N \Delta\rho_j(t_k) f_{ij}(P_i, x_j, y_j, z_j(t_k)), \quad (1)$$

with

$$f_{ij}(P_i, x_j, y_j, z_j(t_k)) = \int_{z_{1j}(t_k)}^{z_{2j}(t_k)} \int_{y_{1j}}^{y_{2j}} \int_{x_{1j}}^{x_{2j}} \frac{z_j(t_k) - z_i(t_k)}{d_{ij}^3} dx_j dy_j dz_j, \quad (2)$$

where γ is the gravitational constant, $\Delta\rho_j(t_k)$ is the time-variable density contrast between the j th prism and its surroundings. N is the number of prisms in the interpretation model. The variable d_{ij} is the distance between the i th measurement point and the j th integration point within the j th prism $(x_j, y_j, z_j(t_k))$:

$$d_{ij} = [(x_i - x_j)^2 + (y_i - y_j)^2 + (z_i(t_k) - z_j(t_k))^2]^{1/2}. \quad (3)$$

Note that in Equations (1)–(3), the vertical coordinates $z_i(t_k)$ and $z_j(t_k)$ are also dependant on time because they can vary in the case of seafloor movement. In Equation (2), the integration is conducted in the variables x_j , y_j , and z_j denoting the x -, y -, and z -coordinates of an arbitrary point belonging to the interior of the j th prism. The integrals limits (Equation (2)) correspond to the j th prism borders in the following way: x_{1j} and x_{2j} are their south and north borders; y_{1j} and y_{2j} are their west and east borders; and z_{1j} and z_{2j} are their depths to the top and bottom. The analytical solution for Equation (1), for a mesh of rectangular prisms, was taken from Nagy et al. [30].

2.2. Reservoir Fluid Substitution and Seafloor Movement Effects

In a hydrocarbon-producing field (gas, oil, or both), the reservoir bulk density is time-variable because of the hydrocarbon removal or its substitution by water or other fluids inside the reservoir. As they have different densities, a time-variable gravity effect is generated. To calculate this effect in a specific position P_i and moment t_k , defined here as $g_z^r(P_i, t_k)$, we represent the reservoir as a mesh of vertical prisms (Figure 2) and use Equation (1). In this case, the density contrast is between the reservoir density at that time ($\rho_j(t_k)$) and the background sediment density (ρ_s).

Another important phenomenon is the seafloor movement caused by hydrocarbon exploitation. If the reservoir pore pressure decreases, it generates reservoir compaction, resulting in the seafloor sinking [16,31–33]. When it occurs, the region of subsidence, initially composed of seafloor sediments in time t_0 (Figure 3a), is replaced by water in time t_1 (Figure 3b) just after the subsidence. We assume that there is only vertical displacement on the seafloor. It means that the i th measurement point on the seafloor in t_0 , $P_i = (x_i, y_i, z_i(t_0))$, changes to $P_i^1 = (x_i, y_i, z_i^1(t_1))$ in t_1 (Figure 3). The opposite occurs when the pore pressure increases.

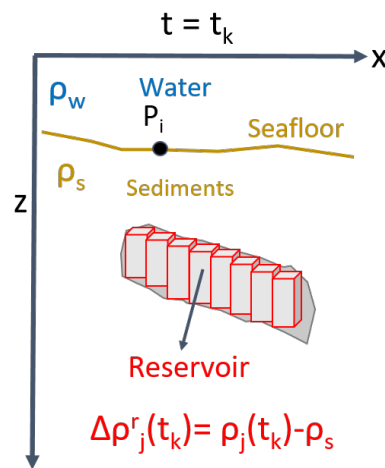


Figure 2. Sketch of a hydrocarbon-producing reservoir (gray prisms) in time $t = t_k$. Its density varies with time due to the substitution of hydrocarbon for water or other fluids inside the reservoir. The observation point P_i is on the seafloor. ρ_w is the water density and ρ_s is the sediment density. $\rho_j(t_k)$ is the density of the j -th prism representing the reservoir in $t = t_k$. $\Delta\rho_j^r(t_k)$ is the density contrast between the j -th prism in the reservoir and its surroundings (sediments) in $t = t_k$.

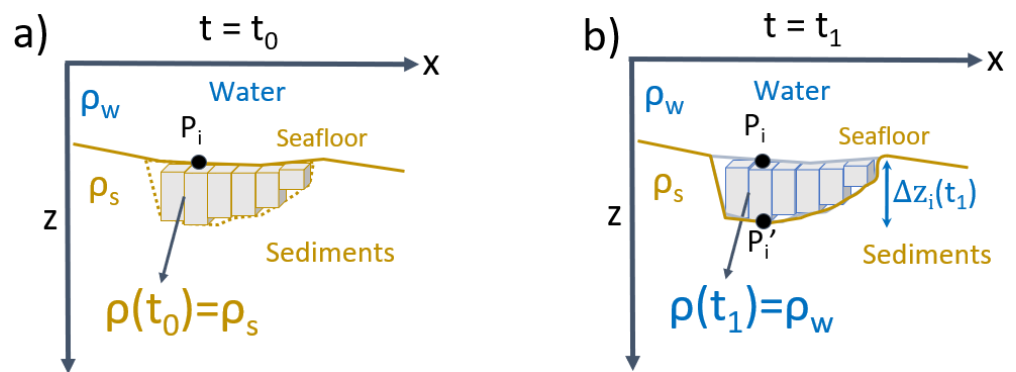


Figure 3. Sketch of a seafloor subsidence process (gray prisms) showing: (a) moment $t = t_0$ before subsidence and (b) moment $t = t_1$ after subsidence. In $t = t_0$, the observation point on the seafloor is P_i and the gray prisms are sediments. In $t = t_1$, this point P_i moved to P'_i , at vertical distance Δz_i from P_i . The region represented by the gray prisms compounded by sediments in t_0 is substituted by water in t_1 .

The change of the seafloor’s vertical coordinates also causes an additional gravity effect that must be taken into account in the modeling calculations once the observation points are on the seafloor. The gravity variation Δg_z^s due to the change of the vertical position in the measurement points (Figure 3) is defined by:

$$\Delta g_z^s = 0.3086\Delta z_i = 0.3086(z'_i(t_1) - z_i(t_0)), \tag{4}$$

where $z_i(t_0)$ is the original vertical coordinate of the observation point P_i (Figure 3a), and $z'_i(t_1)$ is the vertical coordinate of the observation point after the bathymetric change at the point P'_i (Figure 3b). Equation (4) is the free-air gradient used to correct the gravity effect of the vertical distance between the measurement point and the difference in station elevation [29].

The total gravity effect due to seafloor movement, defined here as $g_z^s(P'_i, t_1)$, is the sum of the gravity effect due to the substitution of sediments by water and the free-air gradient (Equation (4)). To calculate the first part, we discretize the new bathymetry region (i.e., the sinking volume after the seafloor movement) into a mesh of vertical prisms (blue prisms in Figure 3b). Then, the gravity effect due to this substitution can be calculated

using Equation (1), where the density contrast is between the seafloor sediments (ρ_s) and the ocean water (ρ_w). If there is a subsidence movement, the density contrast is negative because the ocean water (less dense) substitutes the sediments (more dense). Moreover, if there is an uplift movement, the density contrast is positive.

2.3. Seafloor Movement Estimation

To simulate the seafloor subsidence due to the reservoir compaction in a semi-infinite elastic medium, we selected the strain nucleus concept originally applied in thermodynamics theory [34–37]. The seafloor subsidence Δz_i shown in Figure 3b can be calculated considering the subsurface as a set of strain nuclei that are elements of infinitesimal volume. Once we assume there is no compaction/expansion outside the reservoir, the total subsidence is due to the movement inside the reservoir. Moreover, we consider that there is no change in the reservoir volume, so the compaction is only due to the variation in the reservoir pore pressure. Then, total movement on the seafloor at P_i (Figure 3) is the summation of the movement occurring in the N_r strain nuclei in the reservoir, i.e.,

$$\Delta z(x_i, y_i, z_i(t_0)) = \sum_{j=1}^{N_r} \left[\int \int \int_{V_{1j}} w_{1ij} dV'_j + \int \int \int_{V_{2j}} w_{2ij} dV'_j \right] \quad (5)$$

where w_{1j} represents the infinitesimal vertical displacement in the j th strain nucleus in an infinite medium and w_{2j} is the correction of the vertical displacement considering a semi-space. The second integration in Equation (5) is called the “image nucleus solution” (Figure 4). The infinitesimal vertical displacement in the j th prism and its correction due to j th image nucleus are, respectively, given by:

$$w_{1ij} = \frac{A(1+\nu)}{E} \frac{\partial}{\partial z} \frac{1}{r_{1ij}} \Delta p_j, \quad (6)$$

and

$$w_{2ij} = \frac{A(1+\nu)}{E} \left[2z_i(t_0) \frac{\partial^2}{\partial z^2} \frac{1}{r_{2ij}} - (3-4\nu) \frac{\partial}{\partial z} \frac{1}{r_{2ij}} \right] \Delta p_j, \quad (7)$$

with

$$A = -\frac{c_m E}{4\pi(1+\nu)}, \quad (8)$$

where c_m is the uni-axial compaction coefficient given by:

$$c_m = \frac{(1+\nu)(1-2\nu)}{E(1-\nu)}. \quad (9)$$

E is the Young modulus, ν is the Poisson ratio, and Δp_j is the difference of pore pressure in the j th nucleus between the moments t_0 and t_1 . r_{1ij} and r_{2ij} are the distances from the i -th point (x_i, y_i, z_i) to the j -th strain nucleus (x'_j, y'_j, z'_j) and the j -th image nucleus (x''_j, y''_j, z''_j) , respectively (see Figure 4).

One can note the similarity between the integral functions that describe the gravity anomaly (Equation (1)) and the vertical displacement in a semi-infinite elastic medium (Equation (5)). We solved these equations by using the approach proposed by [37] that have taken advantage of this similarity and used the closed expressions of the gravitational potential and its derivatives produced by the 3D right rectangular prism derived by [30,38] for calculating the displacement field on the seafloor.

Upon calculating the vertical displacement of the seafloor (Equation (5)), we obtain the new bathymetry, that is, the vertical coordinates $z'_i(t_1)$. Then, we use these coordinates in Equation (1) to obtain the gravity anomaly due to the vertical displacement of the seafloor.

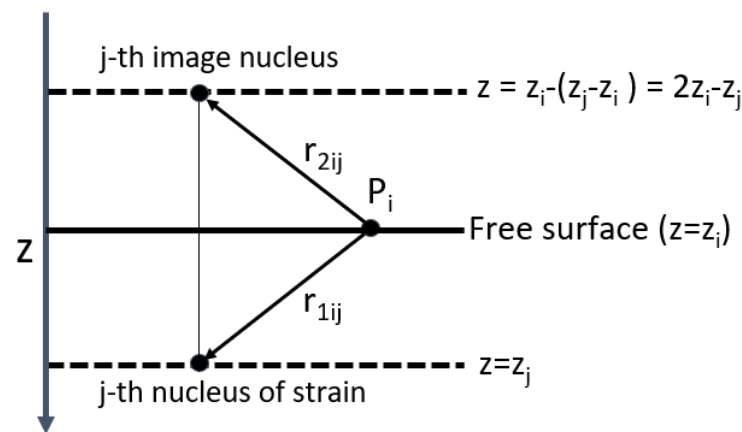


Figure 4. Schematic portrayal of the strain nucleus [31]. The free surface is in $z = z_i$ and the nucleus is in z_j . The observation point P_i is on the free surface and r_{1ij} and r_{2ij} correspond to the distances between the observation point to the strain nucleus and the image nucleus, respectively. According to [32], see chapter 12.

2.4. Four-Dimensional Gravity Anomaly

If there is no movement of the seafloor, the 4D gravity anomaly is the difference of the gravity effect at the station point P_i due to the reservoir production at different times (t_0 and t_1), i.e.,

$$\Delta g_z^{4D}(P_i, t_0, t_1) = g_z^r(P_i, t_1) - g_z^r(P_i, t_0), \quad (10)$$

where the function g_z^r represents the gravity effect of the reservoir region.

Moreover, if we have seafloor subsidence or uplifting (Figure 3b), it is necessary to consider the gravity effect due to these changes on the seafloor. Thus, the 4D gravity anomaly at the measurement point P'_i can be written as:

$$\Delta g_z^{4D}(P_i, P'_i, t_0, t_1) = g_z^s(P'_i, t_1) + g_z^r(P'_i, t_1) - g_z^r(P_i, t_0), \quad (11)$$

where the functions g_z^s and g_z^r , respectively, represent the gravity effects due to seafloor movement and reservoir fluid substitution.

We stress that before the production starts, there is no seafloor movement; hence, the gravity effect in time t_0 is only calculated at the original seafloor (point P_i). Equations (10) and (11) are the main point of this work. For all tested models, we adopted $3 \mu\text{Gal}$ (equivalent to $3 \cdot 10^{-8} \text{ ms}^{-2}$ in SI) as a feasible value to detect the gravity anomalies. This is a conservative value comparing the precision achieved in the present surveys of this type [15,18].

2.5. Campos Basin Geological Setting

Several turbiditic oilfields are situated in the northeastern portion of the offshore Campos Basin, Brazil. The passive margin Campos Basin is one of the predominant Brazilian offshore oil provinces. Its tectonic-sedimentary evolution is associated with the breakup of the Gondwana supercontinent and the opening of the South Atlantic Ocean [39]. It comprises three main tectonic stages: rift, transitional, and drift (Figure 5).

The rift sedimentary sequence includes the Barremian lacustrine deposits of the Lagoa Feia Formation overlaying the Hauterivian (120–130 Ma) Cabiunas basalts. These volcanic rocks characterize the economic basement of the basin. The Lagoa Feia sediments are understood as the principal non-marine source rocks in the Campos Basin [40].

The transitional sequence encloses the Aptian sedimentation, from bottom to top: conglomerates, carbonates, and predominantly the evaporitic rocks deposited during a period of tectonic quiescence. This transitional stage defines the marine drift phase's antecedent, where the sediments are associated with the first seawater invasion via the Walvis Ridge [41].

The drift sequence starts with the Albian/Cenomanian shallow-water calcarenites and calcilitites of the Macaé Formation. They were followed by the Carapebus Formation, a marine Upper Cretaceous to Paleogene deep-water clastic section formed by shale, marls, and sandstone turbidite lenses. These sediments were deposited during general tectonic inactivity and thermal subsidence. The turbidite reservoir systems are sedimented in deep-water settings associated with slope and continental rise deposits [42] and form the most valuable post-salt petroleum reservoirs in the Campos Basin [40]. These turbidites are potential targets for several multi-physics appraisal and monitoring studies [43–45].

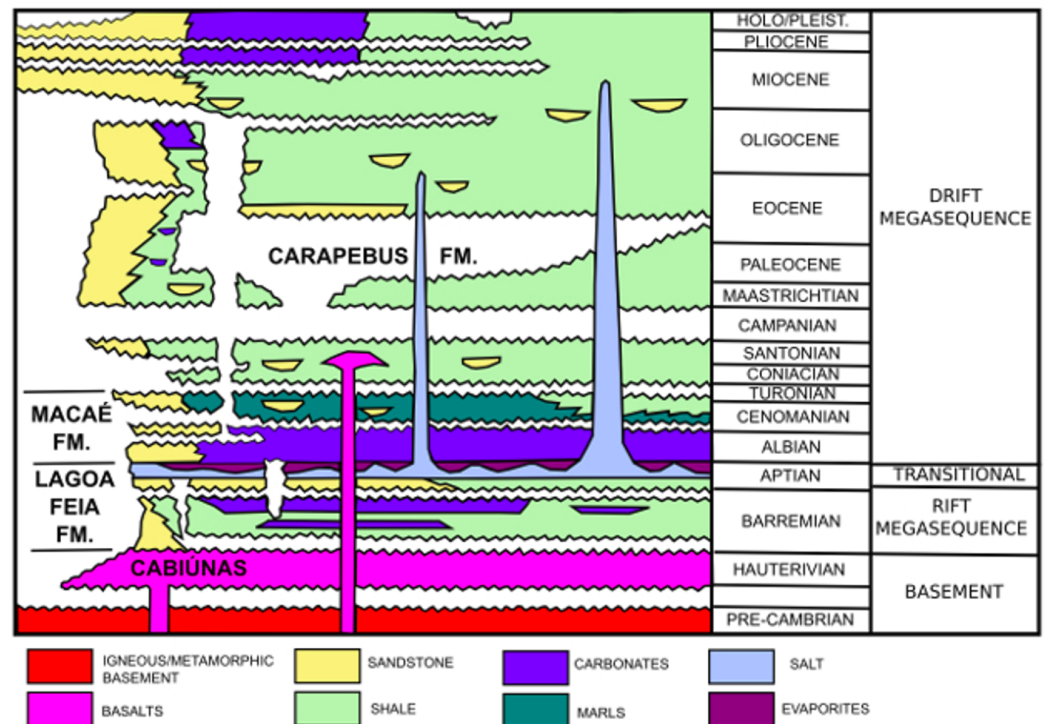


Figure 5. Simplified stratigraphic chart of Campos Basin, modified from [46].

The reservoir model comprises a typical turbiditic reservoir of the Campos Basin. The reservoir facies are thick, up to 300 m, formed by clean, massive, turbidite sandstones interbedded with shales and marls. The trap is of the structural/stratigraphic type. These reservoirs usually have high porosity values in the 26%–32% range [47,48].

2.6. Reservoir Model

The entire interpretation model comprises the extent of 14,050 m in the north axis, 13,250 m in the east axis, and 625 m in the vertical direction. The top and bottom depths are 2712 m and 3337 m deep, respectively. The data relating to the reservoir model (e.g., pore pressure, density, and Poisson's ratio) make up 1,950,312 measurements for each property, with a grid spacing of 50 m along the north and east directions and 25 m in the vertical direction. The data came from reservoir fluid flow simulations for the following years: 2002, 2013, 2014, 2015, and 2018. It is worth noting that the field produces only oil, not gas. The observation points consist of a regular grid of 57 × 54 points in the north and east directions, respectively, with a grid spacing of 250 m in both directions, totaling 3078 observations. The depth of the observation grid is 1338 m deep, the average bathymetry in the oil field region. Over the years, the variation in density has gone from 2.08 to 2.64 g/cm³, and pore pressure data range from 33.2 to 34.2 MPa. The model background has a density of 2.64 g/cm³ and a pore pressure of 0 Mpa, representing the region outside the reservoir. Poisson's ratio data values vary from 0.3237 to 0.3723. Figures 6, 7 and 8 show, respectively, the 3D distributions of density, pore pressure, and Poisson's ratio in 2002.

In order to obtain a better visualization, only the values different from the background are shown.

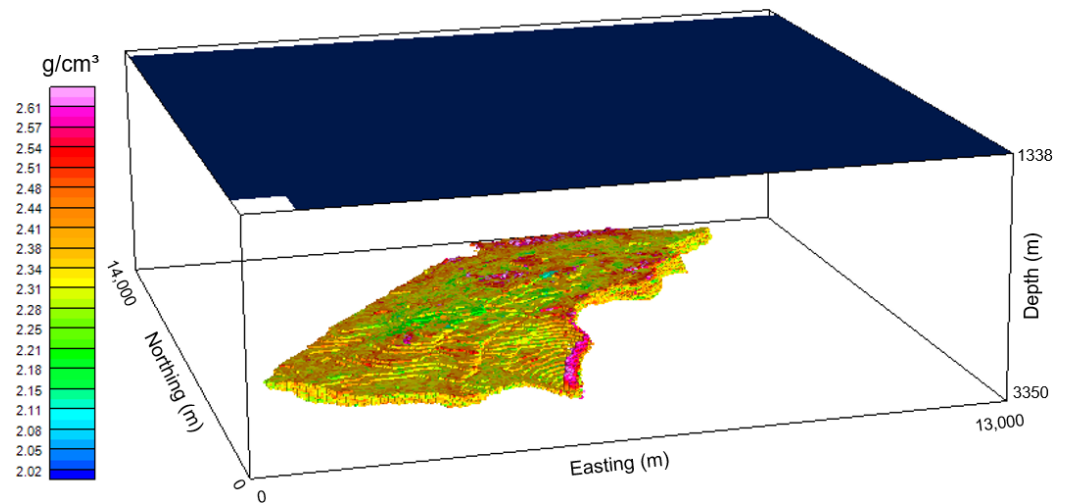


Figure 6. Three-dimensional density data distribution of the turbiditic reservoir model in 2002 (lower volume). The upper surface, with constant bathymetry is the place where the observation points are calculated (Equation (1)).

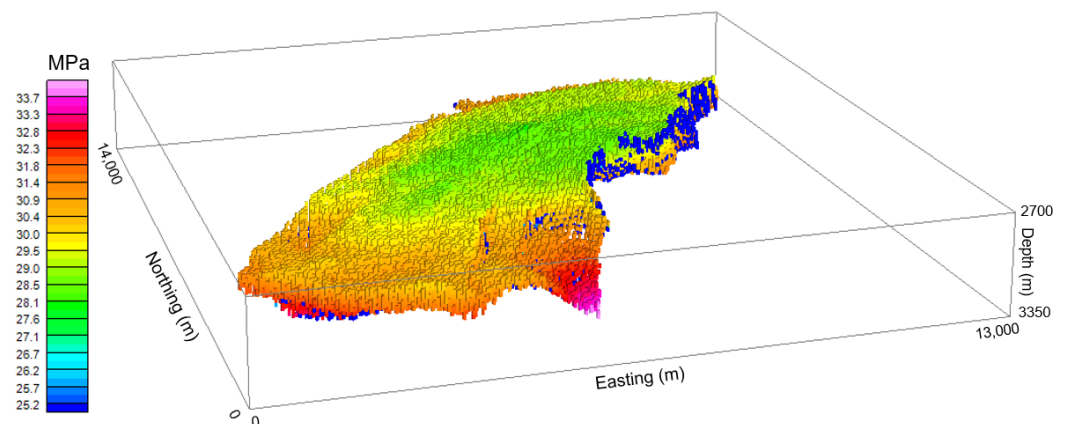


Figure 7. Three-dimensional pore pressure distribution of the turbiditic reservoir model in 2002.

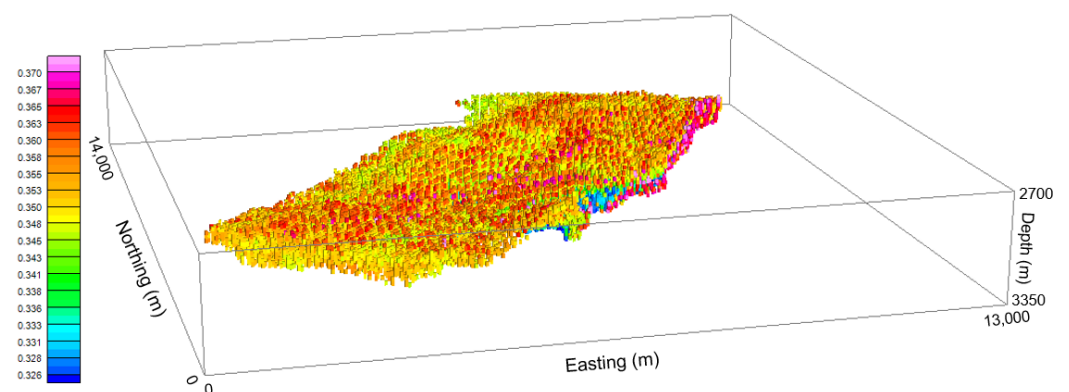


Figure 8. Three-dimensional Poisson ratio distribution of the turbiditic reservoir model in 2002.

3. Results

The results were divided into two groups regarding seafloor movement. The first group shows just one scenario with no seafloor movement, while the second group includes three scenarios where seafloor movement is considered.

3.1. Scenario without Seafloor Movement

In a scenario without seafloor movement, only density changes inside the reservoir are assumed to generate gravity anomalies. Thus, the data used in this scenario are the density differences over the years (Figure 9). Although we do not have information provided by boreholes, we can see an increase in density in the central-northeast region of the area (red arrows in Figure 9), which probably indicates where the production was occurring. This increase is due to the oil replaced with a denser fluid in the reservoir, probably formation water. Only values that are different from zero are shown in Figure 9, which means the colored cells represent where density has changed over the years.

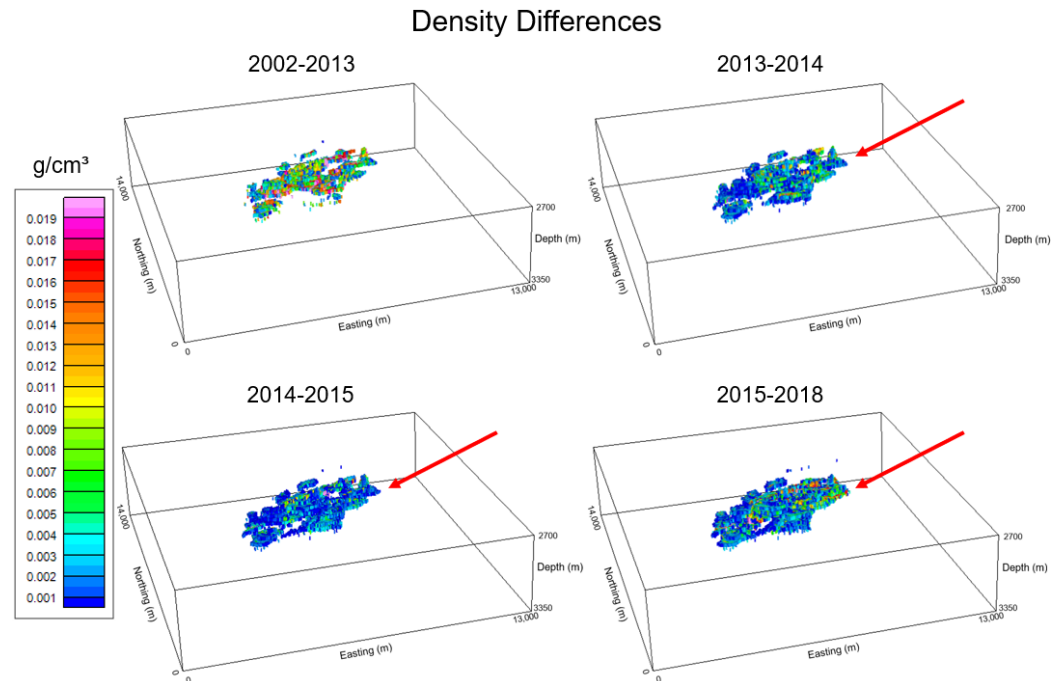


Figure 9. Three-dimensional perspective views of the density differences over the years within the reservoir model (lower volume in Figure 6). Red arrows indicate the region where the density is increasing. Only values that are different from zero are shown.

Using Equation (1), we calculate the gravity anomaly in each year produced by a set of $N_r = 1,861,625$ prisms simulating the reservoir model (lower volume in Figure 6) at the grid of observations located on the seafloor (upper surface in Figure 6). Since the reservoir is less dense than its surroundings, gravity anomalies are negative in all years, reaching a maximum amplitude of more than $1000 \mu\text{Gal}$. The resulting gravity anomalies in each year are not shown because the anomalies are very similar.

Since 2002 is the first year for which we have data, the differences over the years (2013 to 2018) due to density changes within the reservoir (Figure 9) were related to it, producing 4D gravity anomalies (Equation (10)). Figure 10 shows the 4D gravity anomalies over the production years, where we can see that the feasible limit of $3 \mu\text{Gal}$ (dashed red line) is surpassed in 2014 and reaches the amplitude of about $7 \mu\text{Gal}$ in 2018. Thus, according to this scenario, the 4D gravity effect due to oil production (Equation (10)) could be detected after 12 years from the base year.

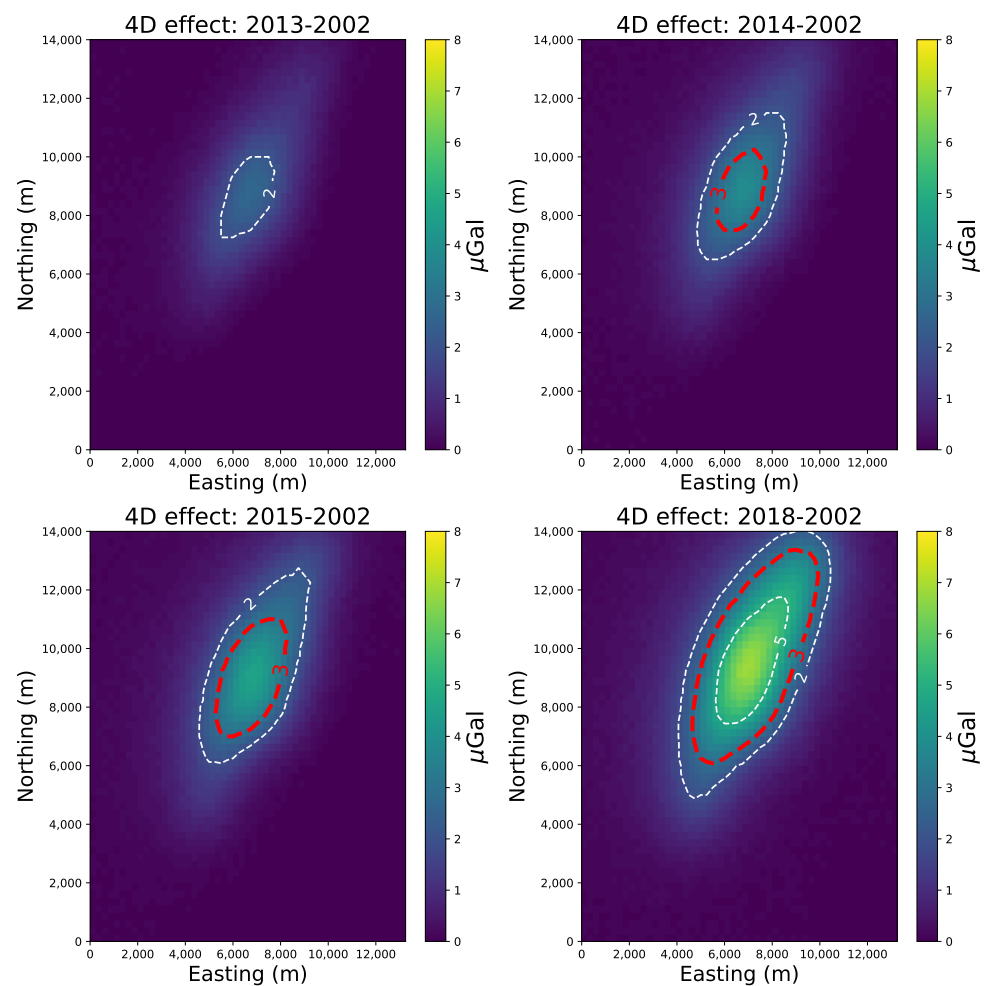


Figure 10. Four-dimensional gravity effect calculated using the reservoir model (lower volume in Figure 6) without seafloor movement. The feasible limit of 3 μGal is represented by the red lines. Observation points are located on the seafloor with a regular spacing of 250 m.

3.2. Scenarios with Seafloor Movement

We also modeled scenarios with seafloor movement calculated using Equation (5), which demands pore pressure and Poisson's ratio data from the reservoir flow simulator. In the case of Poisson's ratio, we choose three possible values according to the original data: 0.33, 0.35, and 0.37. Each value generates different scenarios. We defined Young's modulus as the constant value of 5 GPa related to reservoir sandstone rocks.

The differences over the years in pore pressure distribution (Figure 11) have a more complex pattern than the density differences (Figure 9). For ease of visualization, we split the pore pressure differences (Figure 11) into two parts: negative (left panels) and positive (right panels) parts. Equivalent to Figure 9, Figure 11 shows only cells with values that are different from zero. Note that between 2002 and 2013, the pore pressure differences are only negative and more intense in the same region where the density differences increase (red arrow in Figure 9). From 2013 to 2018, the pore pressure decreased in this region (red arrows in the left panels in Figure 11), but with less intensity and in smaller volume (i.e., a smaller number of model cells). However, pore pressure increased in the southwest region of the model (blue arrows in the right panels in Figure 11) between 2013 and 2018. We believe that this rise in pore pressure is related to fluid injection in the reservoir as a strategy to avoid severe depletion during the production life of the oil field.

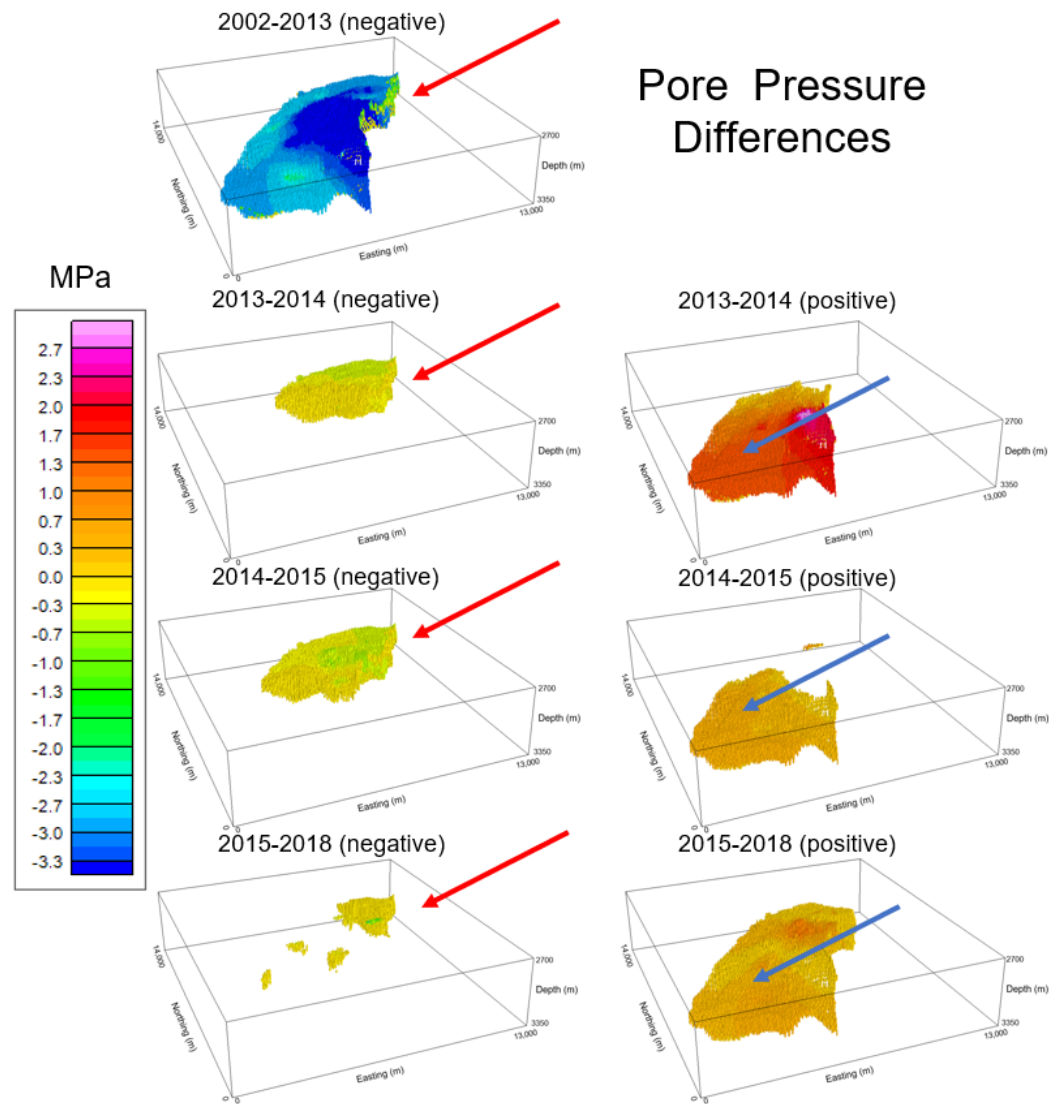


Figure 11. Three-dimensional perspective views of the pore pressure differences over the years from the reservoir model (lower volume in Figure 6). The left and right panels show, respectively, the negative and positive pore pressure differences. Note the pressure has decreased in the central–northeast area since 2013 (red arrows) and has increased in the southwest area since 2014 (blue arrows). Only values that are different from zero are shown.

The modeled seafloor movement in 2013 using three different Poisson ratios can be seen in Figure 12. When Poisson’s ratio rises by 0.02, the amplitude of the seafloor displacement (subsidence or uplift) decreases by about 5 %. Figure 12 also shows small changes in the seafloor relief in the order of a few millimeters. Figure 13 shows that even the lowest value of Poisson’s ratio ($\nu = 0.33$) does not produce seafloor movement greater than 0.6 cm. Between 2013 and 2015, the subsidence (positive values in Figure 13) grows in the central-northeast area while it diminishes in the southwest area. However, between 2015 and 2018, the subsidence in the central-northeast and the southwest regions decreases. As expected, these results are linked to the pore pressure dynamics over the years (Figure 11).

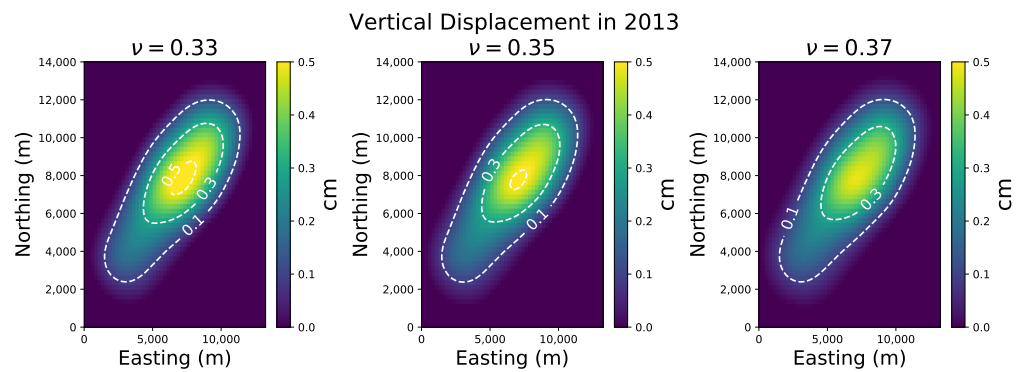


Figure 12. Seafloor movement simulated using Equation (5) for the 2013 year and using three different Poisson ratios (ν). The base year is 2002. Positive values represent the subsidence of the seafloor.

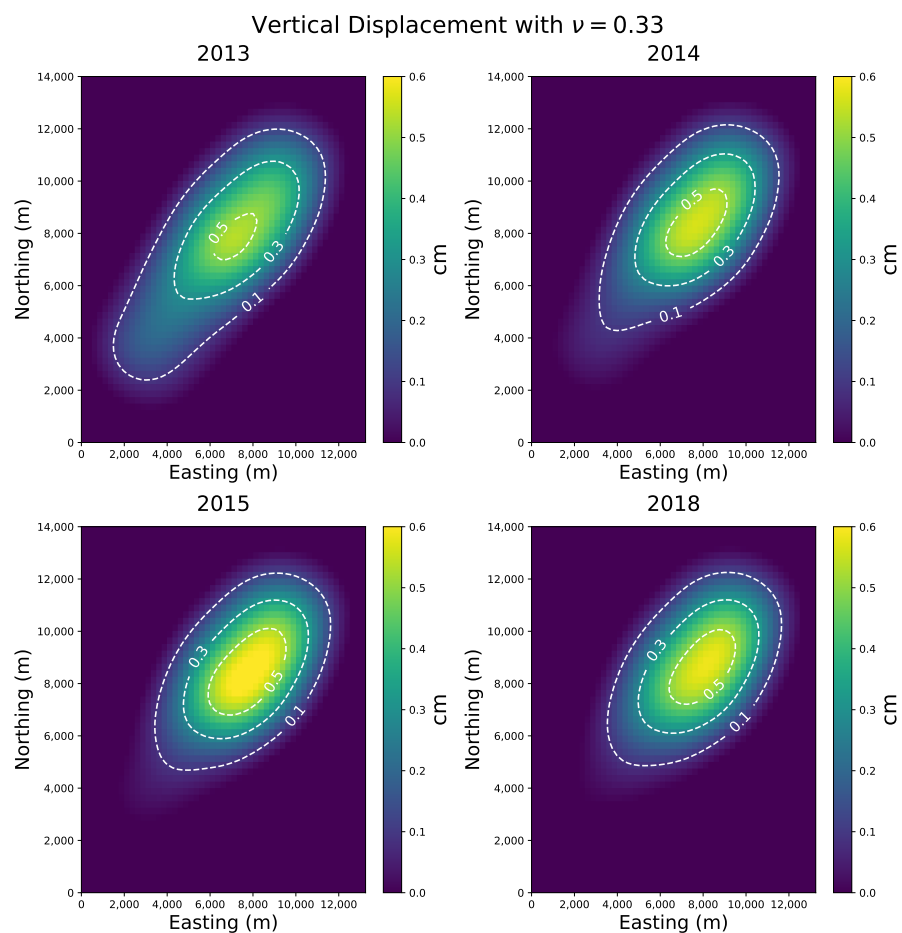


Figure 13. Seafloor vertical displacement simulated by using Equation (5) for years 2013, 2014, 2015, and 2018, for Poisson’s ratio of 0.33. The base year is 2002. Seafloor subsidence is represented by positive values.

Upon estimating the seafloor movement we calculated for each year, the gravity effect due to this phenomenon, which is the sum of the gravity effects from the replacement of sediments by water on the seafloor (Equation (1)) and the free-air correction (Equation (4)). Because 2002 is the base year, we do not have subsidence effect for this year. Figure 14 exemplifies the changes in gravity effect in 2013 due to seafloor movement with $\nu = 0.33$. The shapes of the gravity anomalies concerning the rock/water substitution effect (Figure 14a) and of the vertical correction effect (Figure 14b) have a high correlation with the geometry of the seafloor movement (Figure 13). The rock/water substitution effect

(Figure 14a) is one order of magnitude lower than the vertical correction effect (Figure 14b). In isolation, these two gravity effects (Figure 14a,b) are below the feasible limit of 3 μGal , but the second one is in the same order of magnitude as this limit. The same procedure was repeated for years 2014, 2015, and 2018 with similar results, so they are not shown.

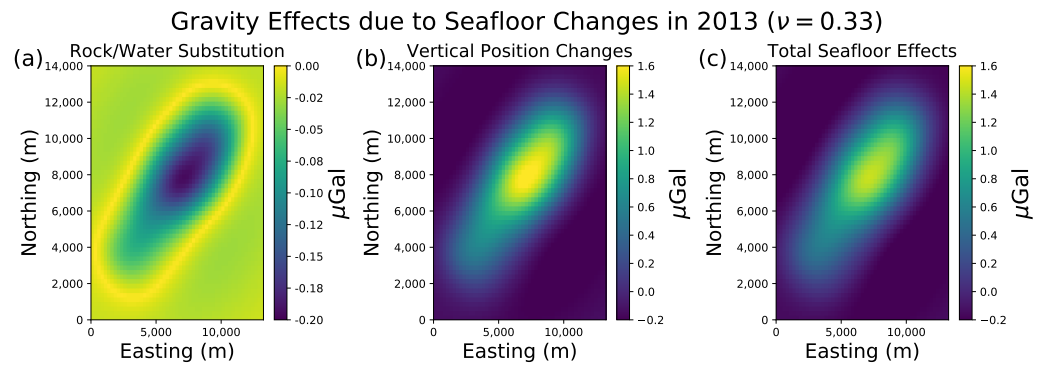


Figure 14. Gravity effect in 2013 due to: (a) rock/water substitution on the seafloor; (b) change of observations' vertical position and; (c) seafloor changes, which is the sum of (a,b). Observation points are located on the seafloor with a regular spacing of 250 m with $\nu = 0.33$.

Using the modified bathymetry, we updated the reservoir gravity effect over the years (with $\nu = 0.33$) to compare with the seafloor change gravity effects. These effects for 2013 are shown in Figure 15, where the total gravity is the sum of the reservoir and seafloor effects. The reservoir effect (Figure 15a) dominates the total gravity effect (Figure 15c) because it is three orders of magnitude greater than the gravity effect due to the seafloor changes (Figures 14c and 15b). The same is valid for other scenarios in different years and with different Poisson ratios.

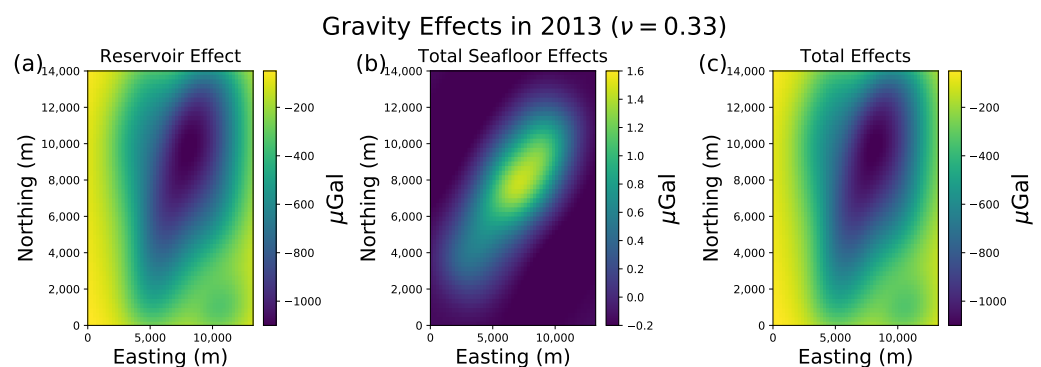


Figure 15. Gravity effect due to: (a) reservoir production; (b) seafloor changes; and (c) the total gravity effect, which is the sum of (a,b). Observation points are located on the seafloor with a regular spacing of 250 m.

At last, we calculated the 4D gravity anomaly over the years (using Equation (11) and $\nu = 0.33$) for the scenarios with seafloor changes. Figure 16 shows that the resulting 4D gravity anomaly is very similar in shape to that of the no-subsidence scenario (Figure 10). However, there is an increase in the maximum anomaly amplitude of about 14 %, which also occurs with the other two Poisson ratios (0.35 and 0.37), although with less intensity. In addition, the 4D gravity anomaly exceeds the feasible limit in 2013 when considering the vertical movement one year earlier than the case with no vertical movement (Figure 10). This result shows that even changes in the seafloor of a few millimeters cannot be neglected. In the Supplementary Material, we conducted tests on synthetic noise-corrupted data to investigate the sensitivity of our method to deal with distinct noise levels (Figures S1–S6).

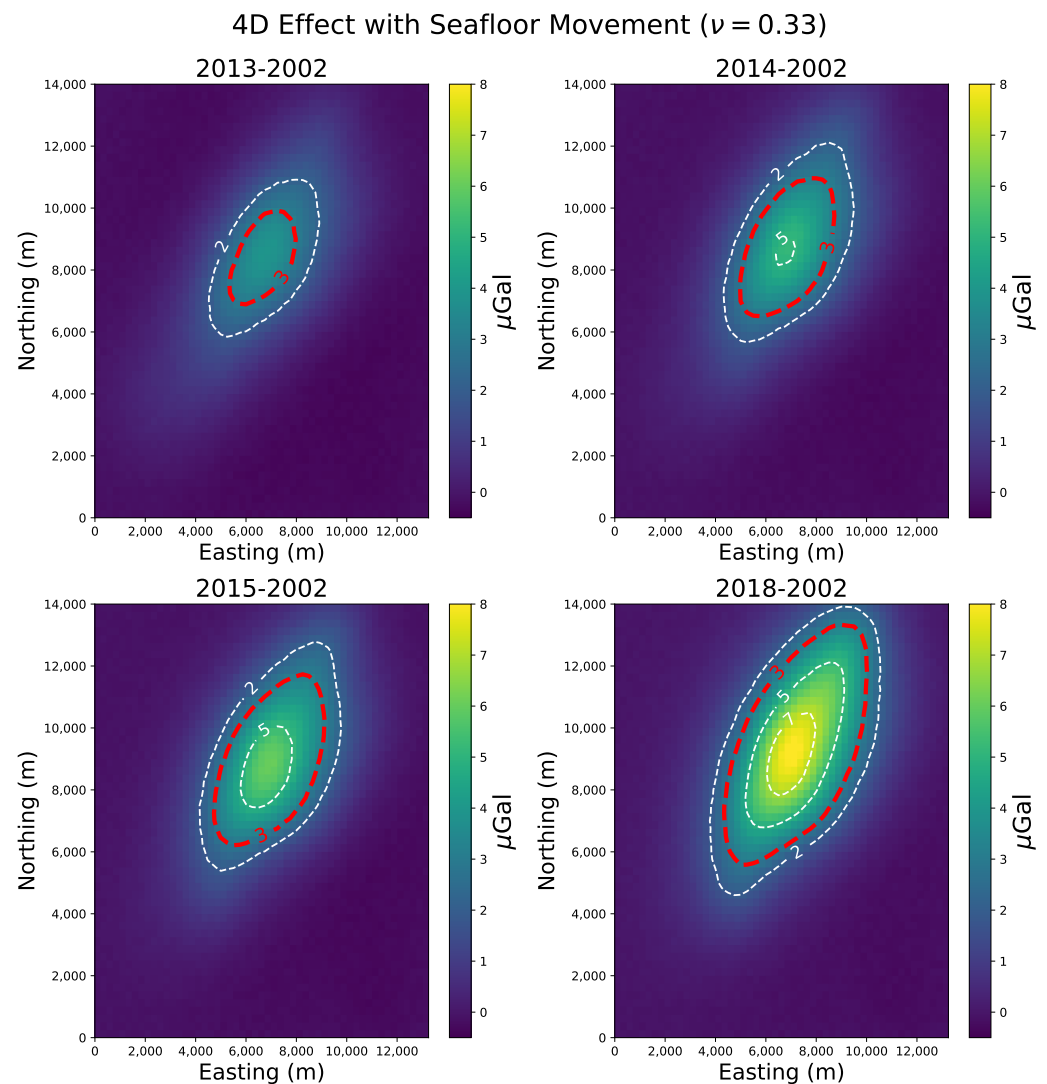


Figure 16. Four-dimensional gravity effect calculated using the reservoir model (lower volume in Figure 6) with seafloor movement (Figure 13). The feasible limit of 3 μGal is represented by the red lines. Observation points are located on the seafloor with a regular spacing of 250 m.

4. Discussion

Density, pore pressure, and Poisson's ratio from a reservoir flow simulator based on a Brazilian hydrocarbon field were the cornerstone information from which we modeled gravity anomalies and seafloor movement between 2002 and 2018. Negative pore pressure and positive density differences in the central-northeast area of the reservoir model suggest the occurrence of oil production there. Moreover, the increase in pore pressure in the southwest area since 2013 could be explained by the beginning of reservoir re-injection as a strategy for oil production. Once there is no density difference in the southwest between 2013 and 2018, the fluid used in this supposed injection could be the formation water or other fluid with the same density.

In this realistic reservoir model, between 2002 and 2018, the 4D gravity anomalies surpass the feasible limit of 3 μGal in the four tested scenarios: one without seafloor movement and three scenarios with subsidence and uplift, varying the Poisson ratios. These modeling results validate the use of 4D gravity measures for monitoring oil production and seafloor movement in considerable depths. In addition, The area of maximum gravity anomaly corresponds to where we suppose hydrocarbon extraction occurs. They also showed that seafloor subsidence leads to a 14 % increase in the 4D gravity anomaly amplitude. According to the methodology, gravity anomalies related to seafloor movement

do not reach the detectability limit ($3 \mu\text{Gal}$) but are in its order of magnitude (between -0.2 and $1.6 \mu\text{Gal}$, Figure 16). The order of magnitude of the time-lapse gravity anomalies calculated in all scenarios of some μGal agrees with the 4D anomalies obtained in real measurements in the North Sea [8,16,19]. We draw the readers' attention to the fact that several parameter combinations related to the reservoir in production could result in detectable anomalies due to seafloor changes. Some examples could be the variations in the Young modulus or the arrangement of density and pore pressure distributions with reservoir volume and depth.

5. Conclusions

Following various and diversified tests using a realistic geophysical model that includes 3D density, pore pressure, and Poisson's ratio distributions, we conclude that the seafloor 4D gravity survey should be beneficial for monitoring the reservoirs of the Brazilian turbiditic fields in deep waters, with or without seafloor movement due to production. There are many active fields already in the Brazilian offshore post-salt that could benefit from this technique. The extension of this work to analyze the feasibility of using 4D gravity acquisitions in the monitoring of reservoirs in Brazilian pre-salt fields has no methodological obstacles.

Supplementary Materials: The following supporting information can be downloaded at: <https://www.mdpi.com/article/10.3390/min13070907/s1>, Figure S1: Noise-corrupted 4D gravity anomaly with zero mean and standard deviation of $0.5 \mu\text{Gal}$ in the scenario without subsidence. Compare with Figure 10 in the article showing the noise-free 4D gravity anomaly. The feasible limit of $3 \mu\text{Gal}$ is represented by the red lines; Figure S2: Noise-corrupted 4D gravity anomaly with zero mean and standard deviation of $0.3 \mu\text{Gal}$ in the scenario without subsidence. Compare with Figure 10 in the article showing the noise-free 4D gravity anomaly. The feasible limit of $3 \mu\text{Gal}$ is represented by the red lines; Figure S3: Noise-corrupted 4D gravity anomaly with zero mean and standard deviation of $0.1 \mu\text{Gal}$ in the scenario without subsidence. Compare with Figure 10 in the article showing the noise-free 4D gravity anomaly. The feasible limit of $3 \mu\text{Gal}$ is represented by the red lines; Figure S4: Noise-corrupted 4D gravity anomaly with zero mean and standard deviation of $0.5 \mu\text{Gal}$ in the scenario with subsidence. Compare with Figure 16 in the article showing the noise-free 4D gravity anomaly. The feasible limit of $3 \mu\text{Gal}$ is represented by the red lines; Figure S5: Noise-corrupted 4D gravity anomaly with zero mean and standard deviation of $0.3 \mu\text{Gal}$ in the scenario with subsidence. Compare with Figure 16 in the article showing the noise-free 4D gravity anomaly. The feasible limit of $3 \mu\text{Gal}$ is represented by the red lines; Figure S6: Noise-corrupted 4D gravity anomaly with zero mean and standard deviation of $0.1 \mu\text{Gal}$ in the scenario with subsidence. Compare with Figure 16 in the article showing the noise-free 4D gravity anomaly. The feasible limit of $3 \mu\text{Gal}$ is represented by the red lines.

Author Contributions: Conceptualization, V.C.F.B. and V.C.O.J.; Methodology, A.D.A., V.C.F.B., V.C.O.J. and P.T.L.M.; Formal analysis, A.D.A.; Investigation, P.T.L.M.; Writing original draft, A.D.A., V.C.F.B., V.C.O.J. and P.T.L.M. All authors have read and agreed to the published version of the manuscript.

Funding: Valeria C.F. Barbosa was supported by fellowships from: CNPQ (grant 309624/2021-5) and FAPERJ (grant E-26/202.582/2019). Vanderlei C. Oliveira Jr was supported by fellowships from CNPQ (grant 315768/2020-7) and FAPERJ (grant E-26/202.729/2018).

Data Availability Statement: Reservoir flow simulator used in this research is classified information.

Acknowledgments: Andre D. Arelaro and Paulo T. L. Menezes thank Petrobras for the permission to publish this work. Valeria C. F. Barbosa and Vanderlei C. Oliveira Jr thank Observatório Nacional, CNPQ, and FAPERJ. All authors thank Julio C.S.O Lyrio, Mariana M. L. Silva, and Luiz A. Santos for the revision of this paper.

Conflicts of Interest: The authors declare no conflict of interest.

References

1. Sasagawa, G.S.; Crawford, W.; Eiken, O.; Noonan, S.; Stenvold, T.; Zumbege, M.A. A new sea-floor gravimeter. *Geophysics* **2003**, *68*, 544–553. [\[CrossRef\]](#)
2. Eiken, O.; Zumbege, M.; Hildebrand, J. Method for Monitoring Seafloor Subsidence and for Gravity Monitoring an Underground Hydrocarbon Reservoir. US Patent 6,813,564, 2 November 2004.
3. Stenvold, T. Offshore Gravimetric and Subsidence Monitoring. Ph.D. Thesis, Norwegian University of Science and Technology, Trondheim, Norway, 2008.
4. Pepper, T. The Gulf underwater gravimeter. *Geophysics* **1941**, *6*, 34–44. [\[CrossRef\]](#)
5. Biegert, E.; Ferguson, J.; Li, X. 4D gravity monitoring—Introduction. *Geophysics* **2008**, *73*, WA1–WA2. [\[CrossRef\]](#)
6. Crossley, D.; Hinderer, J.; Riccardi, U. The measurement of surface gravity. *Rep. Prog. Phys.* **2013**, *76*, 046101. [\[CrossRef\]](#) [\[PubMed\]](#)
7. Zumbege, M.; Alnes, H.; Eiken, O.; Sasagawa, G.; Stenvold, T. Precision of seafloor gravity and pressure measurements for reservoir monitoring. *Geophysics* **2008**, *73*, WA133–WA141. [\[CrossRef\]](#)
8. Alnes, H.; Stenvold, T.; Eiken, O. Experiences on seafloor gravimetric and subsidence monitoring above producing reservoirs. In Proceedings of the 72nd EAGE Conference and Exhibition Incorporating SPE EUROPEC 2010, Barcelona, Spain, 14–17 June 2010; European Association of Geoscientists & Engineers: Utrecht, The Netherlands, 2010; pp. cp–161.
9. Alnes, H.; Eiken, O.; Stenvold, T. Monitoring gas production and CO₂ injection at the Sleipner field using time-lapse gravimetry. *Geophysics* **2008**, *73*, WA155–WA161. [\[CrossRef\]](#)
10. Stenvold, T.; Eiken, O.; Landrø, M. Gravimetric monitoring of gas-reservoir water influx—A combined flow-and gravity-modeling approach. *Geophysics* **2008**, *73*, WA123–WA131. [\[CrossRef\]](#)
11. Eiken, O.; Stenvold, T.; Zumbege, M.; Alnes, H.; Sasagawa, G. Gravimetric monitoring of gas production from the Troll field. *Geophysics* **2008**, *73*, WA149–WA154. [\[CrossRef\]](#)
12. Krahenbuhl, R.A.; Martinez, C.; Li, Y.; Flanagan, G. Time-lapse monitoring of CO₂ sequestration: A site investigation through integration of reservoir properties, seismic imaging, and borehole and surface gravity data. *Geophysics* **2015**, *80*, WA15–WA24. [\[CrossRef\]](#)
13. Røste, T.; Ke, G. Overburden 4D time shifts—Indicating undrained areas and fault transmissibility in the reservoir. *Lead. Edge* **2017**, *36*, 423–430. [\[CrossRef\]](#)
14. Van Camp, M.; Viron, O.; Watlet, A.; Meurers, B.; Francis, O.; Caudron, C. Geophysics From Terrestrial Time-Variable Gravity Measurements. *Rev. Geophys.* **2017**, *55*, 938–992. [\[CrossRef\]](#)
15. Ruiz, H.; Agersborg, R.; Hille, L.; Lien, M.; Lindgård, J.; Vatshelle, M. Monitoring Offshore CO₂ Storage Using Time-lapse Gravity and Seafloor Deformation. In Proceedings of the EAGE/SEG Research Workshop 2017, Trondheim, Norway, 28–31 August 2017; European Association of Geoscientists & Engineers: Bunnik, The Netherlands, 2017; pp. cp–522.
16. Vevatne, J.; Alnes, H.; Eiken, O.; Stenvold, T.; Vassenden, F. Use of field-wide seafloor time-lapse gravity in history matching the Mikkell gas condensate field. In Proceedings of the 74th EAGE Conference and Exhibition Incorporating EUROPEC 2012, Copenhagen, Denmark, 4–7 June 2012; European Association of Geoscientists & Engineers: Bunnik, The Netherlands, 2012; pp. cp–293.
17. Ruiz, H.; Agersborg, R.; Hille, L.; Lindgård, J.E.; Lien, M.; Vatshelle, M. Monitoring offshore reservoirs using 4D gravity and subsidence with improved tide corrections. In *SEG Technical Program Expanded Abstracts 2016*; Society of Exploration Geophysicists: Tulsa, OK, USA, 2016; pp. 2946–2950.
18. Agersborg, R.; Hille, L.; Lien, M.; Lindgård, J.; Ruiz, H.; Vatshelle, M. Density Changes and Reservoir Compaction from In-situ Calibrated 4D Gravity and Subsidence Measured at the Seafloor. In Proceedings of the SPE Annual Technical Conference and Exhibition, San Antonio, TX, USA, 9–11 October 2017; Society of Petroleum Engineers: Richardson, TX, USA, 2017.
19. Vatshelle, M.; Glegola, M.; Lien, M.; Noble, T.; Ruiz, H. Monitoring the Ormen Lange field with 4D gravity and seafloor subsidence. In Proceedings of the 79th EAGE Conference and Exhibition 2017, Paris, France, 12–15 June 2017.
20. Sarkowi, M.; Kadir, W.G.; Santoso, D. Strategy of 4D microgravity survey for the monitoring of fluid dynamics in the subsurface. In Proceedings of the Proceedings World Geothermal Congress, Antalya, Turkey, 24–29 April 2005; pp. 1–5.
21. Ferguson, J.; Chen, T.; Brady, J.; Aiken, C.; Seibert, J. The 4D microgravity method for waterflood surveillance: Part II—Gravity measurements for the Prudhoe Bay reservoir, Alaska. *Geophysics* **2007**, *72*, I33–I43. [\[CrossRef\]](#)
22. Krahenbuhl, R.A.; Li, Y. Time-lapse gravity: A numerical demonstration using robust inversion and joint interpretation of 4D surface and borehole data. *Geophysics* **2012**, *77*, G33–G43. [\[CrossRef\]](#)
23. Krahenbuhl, R.A.; Reitz, A.; Li, Y.; Rim, H. Improved recovery of fluid movement through time-lapse borehole vector gravity. In *SEG Technical Program Expanded Abstracts 2014*; Society of Exploration Geophysicists: Tulsa, OK, USA, 2014; pp. 1348–1353.
24. Young, W.M.; Lumley, D. Feasibility analysis for time-lapse seafloor gravity monitoring of producing gas fields in the Northern Carnarvon Basin, offshore Australia. *Geophysics* **2015**, *80*, WA149–WA160. [\[CrossRef\]](#)
25. Reitz, A.; Krahenbuhl, R.; Li, Y. Feasibility of time-lapse gravity and gravity gradiometry monitoring for steam-assisted gravity drainage reservoirs. *Geophysics* **2015**, *80*, WA99–WA111. [\[CrossRef\]](#)
26. Elliott, E.J.; Braun, A. Gravity monitoring of 4D fluid migration in SAGD reservoirs—Forward modeling. *CSEG Rec.* **2016**, *41*, 16–21.
27. Balza, A.; Li, Y. Integration of time-lapse gravity and production data to monitor gas reservoirs. In Proceedings of the 79th EAGE Conference and Exhibition 2017-Workshops, Paris, France, 12–15 June 2017.

28. Arelaro, A.D.; Barbosa, V.C.; Oliveira Jr., V.C. Seafloor 4D gravity sensitivity analysis of a deep-water Brazilian oil field. In First International Meeting for Applied Geoscience & Energy Expanded Abstracts; Society of Exploration Geophysicists: Tulsa, OK, USA, 2021; pp. 884–888.
29. Blakely, R.J. *Potential Theory in Gravity and Magnetic Applications*; Cambridge University Press: Cambridge, UK, 1996.
30. Nagy, D.; Papp, G.; Benedek, J. The gravitational potential and its derivatives for the prism. *J. Geod.* **2000**, *74*, 552–560. Corrected in *J. Geod.* **2002**, *76*, 475. [[CrossRef](#)]
31. Geertsma, J. Land subsidence above compacting oil and gas reservoirs. *J. Pet. Technol.* **1973**, *25*, 734–744. [[CrossRef](#)]
32. Fjær, E.; Holt, R.M.; Raaen, A.; Horsrud, P. *Petroleum Related Rock Mechanics*; Elsevier: Amsterdam, The Netherlands, 2008.
33. van Thienen-Visser, K.; Pruiksma, J.; Breunese, J. Compaction and subsidence of the Groningen gas field in the Netherlands. *Proc. Int. Assoc. Hydrol. Sci.* **2015**, *372*, 367–373. [[CrossRef](#)]
34. Mindlin, R.D.; Cheng, D.H. Thermoelastic stress in the semi-infinite solid. *J. Appl. Phys.* **1950**, *21*, 931–933. [[CrossRef](#)]
35. Sen, B. Note on the stresses produced by nuclei of thermo-elastic strain in a semi-infinite elastic solid. *Q. Appl. Math.* **1951**, *8*, 365–369. [[CrossRef](#)]
36. Sharma, B.D. Stresses In an Infinite Slab due to a Nucleus of Thermoelastic Strain in it. *ZAMM-J. Appl. Math. Mech. Z. Angew. Math. Mech.* **1956**, *36*, 75–78. [[CrossRef](#)]
37. Barbosa, V.C.F.; Oliveira Jr., V.C.; Arelaro, A.D.; Borges, F.A.S. 3D Displacement and Stress Fields of Compacting Reservoir: Alternative Solutions. *Braz. J. Geophys.* **2022**, *40*, 1–12. [[CrossRef](#)]
38. Fukushima, T. Speed and accuracy improvements in standard algorithm for prismatic gravitational field. *Geophys. J. Int.* **2020**, *222*, 1898–1908. [[CrossRef](#)]
39. Asmus, H.E.; Ponte, F.C. The Brazilian marginal basins. In *The South Atlantic*; Springer: New York, NY, USA, 1973; pp. 87–133.
40. Bruhn, C.; T. Gomes, J.; Lucchese, C., Jr.; Johann, P. Campos Basin: Reservoir Characterization and Management-Historical Overview and Future Challenges. In Proceedings of the Offshore Technology Conference, Houston, TX, USA, 5–8 May 2003.
41. Leyden, R.; Asmus, H.; Zemruscki, S.; Bryan, G. South Atlantic diapiric structures. *AAPG Bull.* **1976**, *60*, 196–212.
42. Freire, W. Campos Basin Deepwater Giant Fields. Paper presented at the Offshore Technology Conference, Houston, TX, USA, 1–4 May 1989. . [[CrossRef](#)]
43. Johann, P.; Sansonowski, R.; Oliveira, R.; Bampi, D. 4D seismic in a heavy-oil, turbidite reservoir offshore Brazil. *Lead. Edge* **2009**, *28*, 718–729. [[CrossRef](#)]
44. Buonora, M.P.P.; Correa, J.L.; Martins, L.S.; Menezes, P.T.L.; Pinho, E.J.C.; Silva Crepaldi, J.L.; Ribas, M.P.P.; Ferreira, S.M.; Freitas, R.C. mCSEM data interpretation for hydrocarbon exploration: A fast interpretation workflow for drilling decision. *Interpretation* **2014**, *2*, SH1–SH11. [[CrossRef](#)]
45. Correa, J.L.; Menezes, P.T. Marlim R3D: A realistic model for controlled-source electromagnetic simulations—Phase 2: The controlled-source electromagnetic data set. *Geophysics* **2019**, *84*, E293–E299. [[CrossRef](#)]
46. Guardado, L.R.; Spadini, A.R.; Brandão, J.S.L.; Mello, M.R. Petroleum System of the Campos Basin, Brazil. In *Petroleum Systems of South Atlantic Margins: AAPG Memoir 73*; Mello, M.R., Katz, B.J., Eds.; AAPG: Tulsa, OK, USA 2000; Chapter 22; pp. 317–324.
47. Rodriguez-Suarez, C.; de Souza, J.A.B.; Sarzenski, D.J.; Ida, M.; Elias, V.L.G. Reservoir characterization of Roncador, Campos Basin. In Proceedings of the 8th International Congress of the Brazilian Geophysical Society, Rio de Janeiro, Brazil, 14–18 September 2003; European Association of Geoscientists & Engineers: Utrecht, The Netherlands, 2003; pp. cp–168.
48. Nascimento, T.M.; Menezes, P.T.; Braga, I.L. High-resolution acoustic impedance inversion to characterize turbidites at Marlim Field, Campos Basin, Brazil. *Interpretation* **2014**, *2*, T143–T153. [[CrossRef](#)]

Disclaimer/Publisher’s Note: The statements, opinions and data contained in all publications are solely those of the individual author(s) and contributor(s) and not of MDPI and/or the editor(s). MDPI and/or the editor(s) disclaim responsibility for any injury to people or property resulting from any ideas, methods, instructions or products referred to in the content.